An Experimental Testbed for Optimization of Data Collection and Analysis in NIRS Functional Neuroimaging

H.L. Graber[1,2], R.L. Barbour[1,2], C.H. Schmitz[3,4], D.C. Lee[2], Y. Xu[1,2]

[1]NIRx Medical Technologies, Glen Head, NY, [2]SUNY Downstate Medical Center, Brooklyn, NY, [3]NIRx Medizintechnik GmbH, Berlin, [4]Charité Univeritätsmedizin, Berlin

Abstract

Invasive electrode recordings currently are the most important source of information regarding the brain's neural activity. Noninvasive methods would offer numerous advantages, including access to a larger fraction of the brain. Furthermore, recent results demonstrate that functional near infrared spectroscopic (fNIRS) imaging can probe cortical function with spatial resolution sufficient to localize neural activation to the correct cortical locus, with fewer motility constraints than are commonly associated with, e.g., functional magnetic resonance imaging (fMRI). We are developing a closed-loop testbed for optimizing the utility of fNIRS measurements, alone or in conjunction with EEG measurements, as a method for studying brain function. The essential components include solid-state, programmable, dynamic phantoms for fNIRS or simultaneous fNIRS/EEG measurements, in human or primate subjects. This hardware component allows users to directly evaluate the accuracy, robustness, speed, and other performance characteristics of data analysis strategies applied to noninvasive neuroimaging data. The complementary software component includes a set of anatomical atlases for human and primate functional neuroimaging. These are 3D representations of the heads of standardized subjects that improve the accuracy and spatial resolution of recovered images by taking the details of the inhomogeneous, irregularly shaped, anatomy into account, and their use minimizes the effects of inter-subject variations. Presented results demonstrate the utility of the testbed for assessing the temporal and spatial accuracy of information in recovered images, and for characterizing algorithms that are used in studies on the effective connectivity among mutually interacting cortical regions.

Introduction

- Among the many applications proposed for functional near infrared spectroscopic (fNIRS) imaging, neuroimaging currently is the focus of a large fraction of research and development efforts
  - Reasons for the interest in fNIRS imaging include that it has the spatial resolution needed to localize activation in the somatosensory cortex [1], and it is more mobile than other non-invasive methods [2].
  - As described in an accompanying poster, fNIRS imaging also readily lends itself to consideration of simultaneous dual-mode neuroimaging methods. Of particular interest is combining fNIRS and EEG.
- As is the case for any functional imaging application, in fNIRS or fNIRs-EEG it is necessary to develop methods to assess the accuracy of recovered spatial and temporal information.
  - Functional properties do not necessarily have obvious anatomical correlates.
  - Consequently, there would be considerable value in a tool that would allow researchers or practitioners to conduct tests of functional imaging algorithms with a priori knowledge of the "ground truth."
- Here we present a testbed for fNIRS imaging, which includes a stable solid-state phantom containing embedded electrochromic and electric-dipole elements.
  - The behavior of the internal devices are user-controlled and programmable, such that the electrochromic and electric-dipole elements can be used to mimic position-dependent and time-varying hemodynamic and bioelectric responses to neural activity, respectively.
  - Additional aspects of the testbed include a support environment for the phantom, including integrated sensing headgear and a robust data analysis environment.
- In comparison to simulation-based studies of algorithm performance, the testbed allows one to employ for evaluation purposes the same imaging systems and measurement heads as are intended for the experimental or clinical studies.
  - Therefore, factors such as optical coupling, electronic noise, inter-channel crosstalk, and serial autocorrelation all are precisely the same in the assessment phase as they would be under conditions of actual use.

Methods

- Solid-State Dynamic Phantom (Fig. 1)
  - Anthropomorphic (or other biological forms (see Fig. 5A)), air-tight, and resistant to biological degradation
  - Matrix consists of silicone and saline-based biopolymer
  - Electrochromic cells (ECC) mimic wavelength-dependent hemodynamic responses
  - Electric dipoles mimic bioelectric responses
  - Connectors for user interface and controlling electronics are built into the base of the phantom (see Fig. 2B,C).
- Sensing and Headgear
  - NIRx NIRScout imaging system
    - Accommodates up to 32 detectors and 48 sources, time-multiplexed with adjustable gain switching [2,5]
    - 16 detectors and 16 dual-wavelength superluminescent LEDs operating at 760 and 850 nm were used
  - NIRx DYNOT Compact imaging system
    - Accommodates up to 32 detectors and 9 sources, time-multiplexed with adjustable gain switching
    - 30 detectors and 9 dual-wavelength diode-laser sources operating at 760 and 830 nm were used
  - Headgear in either case was a modified Brain Products Easy-Cap (Fig. 2) [6]
- NAVI-SPM and Mapping Environment
  - NAVI (Near-Infrared, Analysis, Visualization and Imaging) [7,8]
    - Extensive data-editing functionality
    - FEM-based image formation (Fig. 3)
  - Various display options, including Automated Anatomical Labeling (AAL) method employed by SPM [9]
  - GLM methods used in support of individual (level 1) and group (level 2) analysis for detection of neuroactivation
  - Atlas-based mapping environment in support of human and macaque studies (Fig. 4)
    - Serves as basis for rapid 3D image reconstruction
- Dynamic Causal Modeling (DCM)
  - Mathematical strategy for analyzing functional neuroimaging data in order infer effective connectivity [3,4]
  - Chosen over approaches that are exclusively data-driven, because model selection can be reliably guided by prior knowledge [10]

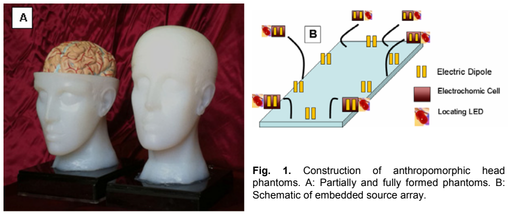

Fig. 1. Construction of anthropomorphic head phantoms. A: Partially and fully formed phantoms. B: Schematic of embedded source array.

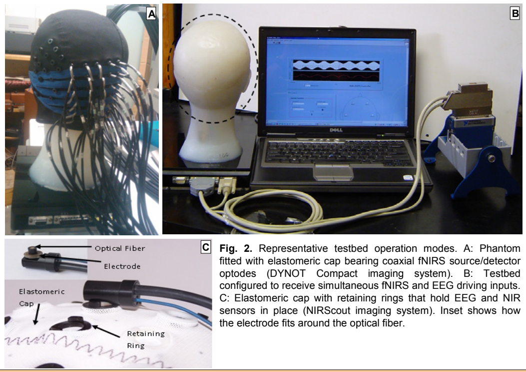

Fig. 2. Representative testbed operation modes. A: Phantom fitted with elastomeric cap bearing coaxial fNIRS source/detector optodes (DYNOT Compact imaging system). B: Testbed configured to receive simultaneous fNIRS and EEG driving inputs. C: Elastomeric cap with retaining rings that hold EEG and NIR sensors in place (NIRScout imaging system). Inset shows how the electrode fits around the optical fiber.

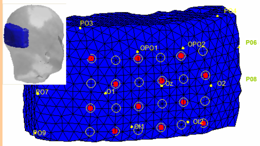

Fig. 3. Exemplary FEM mesh from the human-head atlas. A representative arrangement of optodes also is shown. Open circles indicate detector-only fibers; filled circles are co-located source-detectors. Yellow dots are locations of standard EEG electrodes.

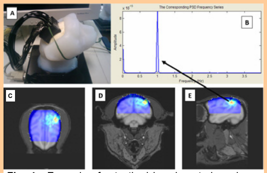

Fig. 4. Example of a testbed imaging study, using a macaque head-shaped dynamic phantom. A: the phantom with fibers attached. C-E: horizontal, coronal and sagittal views of a recovered image, with the ECC accurately located. D: the 1 Hz sinusoidal driving function is recovered with negligible distortion.

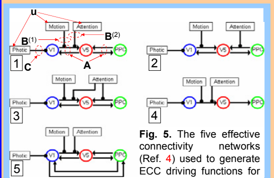

Fig. 5. The five effective connectivity networks (Ref. 4) used to generate ECC driving functions for the dynamic phantom. Connections that correspond to matrices in Eq. (1) are labeled.

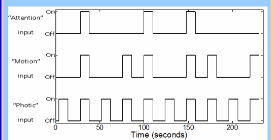

Fig. 6. Modeled time courses for exogenous inputs **u** in Eq. (1).

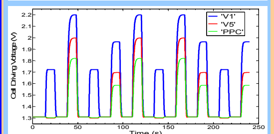

Fig. 7. Time courses of the driving voltages used to model the hemodynamic responses of the indicated cortical regions.

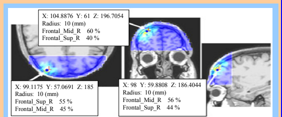

Fig. 8. Spatial localization of an ECC in the human-head phantom. Plotted quantity is the GLM β coefficient obtained by fitting a driving function to the image time series in each pixel.

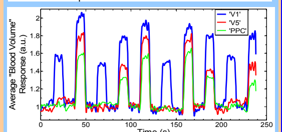

Fig. 9. Time courses of the hemodynamic responses recovered from the image time series, for each ECC driving function (cf. Fig. 7).

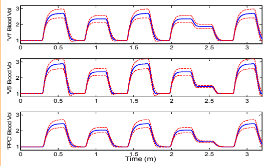

Fig. 10. Sensitivity of Eq. (2) solution to small perturbations of the neurovascular coupling parameters

Methods (cont.)

- Experimental study of DCM model selection accuracy, based on analysis of fNIRS time series imaging data
  - Bilinear mathematical model of temporally evolving neuronal activity [4]:

$$\frac{d\mathbf{x}}{dt} = \left[\mathbf{A} + \sum_j u_j \mathbf{B}^{(j)}\right]\mathbf{x} + \mathbf{C}\,\mathbf{u}. \qquad (1)$$

  - **x** = time-varying neural activity in a user-specified number of cortical regions
- **A**, **B** and **C** matrices in Eq. (1) specify the effective connectivity, i.e., the effects that activity in one region has on others, and the effects of exogenous inputs **u** on neural activity. (**Fig. 5**)
- For each cortical region, the hemodynamic response to a given value x of neural activity is estimated by means of a neurovascular coupling model [3,8]:

$$\begin{aligned} ds/dt &= x - \kappa s - \gamma\,(f-1), \\ df/dt &= s, \qquad dv/dt = \left(f - v^{1/\alpha}\right)\big/\tau, \\ dq/dt &= \left\{\left[1-(1-E_0)^{1/f}\right]f\big/E_0 - (q/v)\,v^{1/\alpha}\right\}\big/\tau. \end{aligned} \qquad (2)$$

  - s = vasodilatory signal, f = blood flow, q = deoxyhemoglobin content, v = blood volume; κ = vasodilatory signal decay rate, γ = autoregulatory feedback rate constant, τ = mean capillary transit time, α = vessel stiffness exponent, E_0 = capillary resting net oxygen extraction.
- The values of **u** are time-dependent; given the particular **u** in **Fig. 6** and the connectivity pattern depicted in the upper left of **Fig. 5**, solving the coupled differential equations in Eqs. (1) and (2) yields the **v** time series potted in **Fig. 7**.
  - As indicated in **Fig. 7**, the computed **v** time series are used as time-varying voltage signals that drive the ECCs in the dynamic phantom.
  - Higher voltage → darker ECC → lower intensity of light detected in an fNIRS measurement. This mimics the effect of an increase in cerebral blood volume.

Results

- Five sets of fNIRS measurements were carried out, using ECC driving functions computed for each of the models in **Fig. 5**.
- Analyzing the data with NAVI-SPM, using GLM methods from Level-1 SPM, yields statistical parametric maps, such as those shown in **Fig. 8**.
- A spatial mean time series result was generated for each of the driving functions (e.g., **Fig. 7**); subsequently, these served as the input for DCM inverse-problem computations.
  - For each set of experiment-derived data, all five models in **Fig. 5** were evaluated as effective connectivity hypotheses.
  - Based on comparisons of the computed Bayesian evidence (Ref. 4) for each hypothesis, the correct connectivity hypothesis was selected in only two of the five cases (Models 2 and 3).
  - Additionally, examination of measurement-data replicates showed that inverse-problem results [i.e., Bayesian evidences, estimated values for the connectivity matrices in Eq. (1)] are substantially less repeatable than the spatiotemporal imaging results (Figs. 8,9).
- The preceding result suggests the utility of performing additional forward-problem modeling studies, to evaluate the sensitivity of the principal output variables of the hemodynamic model [q and v in Eq. (2)] to uncertainties in the values of the neurovascular coupling parameters [α, γ, κ, ρ and τ in Eq. (2)].
  - Modeled each parameter as a Gaussian random variable: $\alpha = \alpha_0[1 + N(0,0.1)]$, etc.
  - Numerically integrated Eq. (2), for 500 sets of parameter values and a fixed solution to Eq. (1).
- In 67±3 of the 500 trials, forward problem solution was unstable, increasing without bound.
  - For the remaining trials, the average solution (Fig. 10, blue curves) was indistinguishable from the solution of the unperturbed equation. But the solution amplitudes vary over a substantial range (Fig. 10, red curves).
  - The trials for which the numerical solution did not converge exhibit a characteristic pattern of parameter values: cases in which α, γ, κ and τ simultaneously have lower-than-average (by 3-10%) values
    - Physiologically, $\alpha\downarrow$ corresponds to increased venous outflow; $\gamma\downarrow$, $\kappa\downarrow$ both correspond to increased production of vasodilatory signal; $\tau\downarrow$ corresponds to decreased mean capillary transit time.

Conclusion

- An issue of central importance for fNIRS or fNIRS-EEG imaging analysis is establishing the accuracy of computed solutions. To accomplish this it is necessary to have an ability to design situations where the "ground truth" is unequivocally known a priori. The availability of an experimental testbed, such as the one described here, facilitates the development and testing of algorithms for analysis of functional neuroimaging data.

References

1. Koch, S.P., Habermehl, C., Mehnert, J., Schmitz, C.H., Holtze, S., Villringer, A., Steinbrink, J., Obrig, H. (2010), 'High-resolution optical functional mapping of the human somatosensory cortex', Frontiers in Neuroenergetics, vol. 2, Article 12.
2. Schmitz, C.H., Koch, S.P. (2009), 'Ultracompact, EEG-compatible NIRS system', Poster C 05 at the Berlin Brain Computer Interface Workshop.
3. Friston, K.J., Harrison, L., Penny, W. (2003), 'Dynamic causal modelling', NeuroImage, vol. 19, pp. 1273-1302.
4. Penny, W.B., Stephan, K.E., Mechelli, A., Friston, K.J. (2004), 'Comparing dynamic causal models', NeuroImage, vol. 22, pp. 1157-1172.
5. http://www.nirx.net/uploads/Brochures/NIRx_NIRScout.pdf.
6. http://www.brainproducts.com/productdetails.php?id=28&tab=1.
7. Pei, Y., Xu, Y., Barbour, R.L. (2007), 'NAVI-SciPort solution: A problem solving environment (PSE) for NIRS data analysis', Poster No. 221 M-AM at Human Brain Mapping (Chicago, IL, June 10-14, 2007). Available: http://otg.downstate.edu/Publication/PeiHBM07.pdf.
8. NIRx fNIRS Analysis Environment User's guide. Available: http://otg.downstate.edu/Publication/NIRxPackage_02.pdf.
9. Tzourio-Mazoyer, N., Landeau, B., Papathanassiou, D., Crivello, F., Etard, O., Delcroix, N., Mazoyer, B., Joliot, M. (2010), 'Automated anatomical labeling of activations in SPM using a macroscopic anatomical parcellation on the MNI MRI single-subject brain', NeuroImage, vol. 15, pp. 273-289.
10. Friston, K. (2009), 'Causal modeling and brain connectivity in functional magnetic resonance imaging', PLoS Biology, vol. 7, pp. 0220-0225.

Acknowledgements

This work was supported by the Defense Advanced Research Projects Agency; by the NIH under grant nos. R21NS067278, R42NS050007 and 5R44NS049734; by the New York State Department of Health; and by EU grants NEST 012778, EFRE 200020062/6, and nEUROpt 201076.